Journal of Energy Chemistry 72 (2022) 81–87

Contents lists available at ScienceDirect

Journal of Energy Chemistry

journal homepage: www.elsevier.com/locate/jechem

http://www.journals.elsevier.com/journal-of-energy-chemistry/

Anode reaction mechanisms of Na|NaCl-$CaCl_2$|Zn liquid metal battery

Fang Zhang [a], Jingyun Jin [a], Junli Xu [b,1,*], Zhongning Shi [c,1,*]

[a] School of Metallurgy, Northeastern University, Shenyang 110819, Liaoning, China
[b] College of Sciences, Northeastern University, Shenyang 110819, Liaoning, China
[c] State Key Laboratory of Rolling and Automation, Northeastern University, Shenyang 110819, Liaoning, China

ARTICLE INFO

Article history:
Received 4 January 2022
Revised 20 April 2022
Accepted 22 April 2022
Available online 30 April 2022

Keywords:
Liquid metal battery
Thermodynamic calculation
Discharge plateaus
Reaction mechanisms
Ca-Zn intermetallic compounds

ABSTRACT

Na|NaCl-$CaCl_2$|Zn liquid metal battery is regarded as a promising energy storage system for power grids. Despite intensive attempts to present a real mechanism of metal electrodes reaction, those for Na||Zn LMBs are not clear yet. Herein, the anode reactions for the multiple discharge potential plateaus were deduced by means of FactSage thermochemical software, which were subsequently validated by X-ray diffraction analysis and the modeling of phase transformation in the cooling process. A pre-treatment process was proposed for the analysis of anode product composition using the atomic absorption spectrometry method, and the anode states at working temperature (560 °C) were obtained by the Na-Ca-Zn ternary phase for the first time. The results indicate the discharge of Na and Ca led to the formation of Ca-Zn intermetallic compounds, whilst the extraction of Ca in Ca-Zn intermetallic compounds was responsible for the multiple discharge plateaus. Moreover, it was found that the charging product was in electrochemical double liquid metal layers, which are composed of Na and Ca with dissolved Zn respectively.

1. Introduction

Countries all over the world have strengthened the development and utilization of renewable energy sources such as wind and solar energy in response to the growing concerns over carbon footprint and environmental policies and climate change [1–3]. However, large-scale energy storage devices are required to harness the potential of solar and wind energy and to bring out an enhanced utilization of the intermittence renewable energy sources. Batteries can provide a low-cost way of energy production, renewable energy storage, and excellent key technology in the world's transition to the green energy system [4]. Large-scale batteries are the key factor in this transition and remain the main grid-based energy storage devices because of their unlimited landform, easy expansion, and cheap maintenance cost [5–8]. Moreover, long-lasting and stable batteries can provide greater flexibility for the grid and reduce carbon emissions [9,10]. In recent decades, liquid metal batteries (LMBs) have attracted wide attention due to their fast liquid–liquid interface dynamics, high ionic conductivity, and high cycle stability, which have great application potential for large-scale energy storage [11–13].

The insight for high-temperature liquid metal batteries (HTLMBs) traces back to the early 1900 s, and they had begun to be actively researched by national laboratories and industry since the 1960 s before being reintroduced at MIT in the 2000 s [14,15]. These batteries are assembled from metal anodes which can be alkali metals, alkaline earth metals, or first-row transition metals (e.g., A: Li, Na, Mg, Ca, Zn) and A-B, or A-B-C alloy cathode in a proper electrolyte that makes the LMB. Thus, anode A loses electrons during the discharge process and enters the electrolyte as A^{Z+} ions. Meanwhile, A^{Z+} ions in the electrolyte get electrons at the cathode surface and diffuse into B metal (or B-C alloy) to form A-B (A-B-C) cathodes. Conceptually, the thermodynamic driving force for cell discharge can be interpreted as emanating from a strong interaction between A and B, in which A's activity can be extremely low ($a_{A(\text{in B})}$ can be as low as 10^{-10}) [11]. Various types of LMBs have been developed to date, including Na||Sn [16], K||Hg [17], Na||Hg [18–20], Na||Bi [21], Mg|| (Mg-Sb) [12], Li|| (Li-Sb-Pb) [22], Li|| (Li-Sb-Sn) [23], (Li-Pb) ||Pb [24,25], (Ca-Mg) || (Ca-Mg-Bi) [26], Sn||Bi [27], Li|| (Li-Sb-Bi) [28], Li|| (Bi-Pb) [29], (Zn-Sn) ||Bi [30], Li||Te, Na||Te, K||Te, and Li|| (Te-Sn) [31] LMBs. The full liquid structure enables the LMB to work as high as 1300 mA cm^{-2} current density with a coulombic efficiency of 100% [32,33].

Xu et al. [34,35] have reported a membrane-free Na|NaCl-$CaCl_2$|Zn LMB (Na||Zn LMBs) at 560 °C. The battery was assembled in a completely discharged state. Only metallic Zn and NaCl-$CaCl_2$

* Corresponding authors.
E-mail addresses: jlxu@mail.neu.edu.cn (J. Xu), znshi@mail.neu.edu.cn (Z. Shi).
[1] These authors contributed equally to this work.

https://doi.org/10.1016/j.jechem.2022.04.035

electrolytes were needed to assemble the battery. Anode material (metallic Na) was produced during the charging process. The battery was safe, environmentally friendly, and inexpensive since Zn, NaCl, and $CaCl_2$ are all abundant, have high chemical stability, and are nontoxic. Furthermore, Na|NaCl-$CaCl_2$|Zn has a higher discharge voltage than other known LMBs. In the aforementioned study, the discharge voltage was about 1.1 V at 100 mA cm^{-2}. The electrode reaction proposed by the authors is as follows.

$$\text{Anode}: \ Na - e^- \leftrightarrow Na^+ \tag{1}$$

$$\text{Cathode}: \ Zn^{2+} + 2e^- \leftrightarrow Zn \tag{2}$$

The cell voltage depends on the gap between the anode (Na) and cathode (Zn) potentials, for a theoretical discharge voltage set to approximately 2.0 V. The cell voltage difference at different current densities is due to polarization's effect. However, the observations have revealed the existence of 4 discharge plateaus at 10 mA cm^{-2}, indicating the complexity of the electrode reaction, which is not as simple as depicted in the previously proposed reaction. Therefore, further investigations are needed to elucidate the underlying mechanism.

In this work, Na|NaCl-$CaCl_2$|Zn was assembled in a completely discharged condition, and it underwent charging/discharging at various current densities. The electrode products at different charge–discharge states were collected and analyzed with versatile tools such as scanning electron microscopy (SEM), the energy-dispersive X-ray spectroscopy (EDS), X-ray diffraction (XRD), and finally with the atomic absorption spectroscopy (AAS). The electrode reactions describing the charge–discharge processes are suggested by merging the useful information from the phase diagram analysis and the experimental results.

2. Experimental

2.1. Pretreatment of molten salt electrolyte

Equimolar NaCl-$CaCl_2$ mixture was used as electrolyte. Analytical reagents NaCl (99.8%) and $CaCl_2$ (99.0%) were purchased from China National Pharmaceutical. The salt mixture was dried under vacuum at 400 °C for 4 h to remove residual water and then melted at 560 °C for 2 h under argon atmosphere before use.

2.2. Cell assembly and testing

All batteries were assembled in a glove box filled with argon. A graphite crucible (inter diameter (ID): 39 mm, height (H): 125 mm, sidewall thickness: 4 mm) with an insulating alumina tube inside was used as the battery container, which has good stability in corrosive molten chloride [36,37]. 20 g Zn metallic particles (98%, China National Pharmaceutical) were placed at the bottom of the graphite crucible with an insulating alumina tube. Then, 120 g equimolar NaCl-$CaCl_2$ mixture was added upon Zn metallic particles. A steel wire connected to the graphite crucible is acted as a cathode current collector, while a molybdenum wire ($\varphi 1 \times 900$ mm) inserted into the NaCl-$CaCl_2$ electrolyte is used as an anode current collector. The diagram of the cell is shown in Fig. 1. The assembled cell was heated up at 10 °C per minute and held at 300 °C for 2 h to further remove moisture, and then it was heated at 560 °C for 2 h before electrochemical tests. The constant current charge-discharge performance was tested in an argon atmosphere using a LAND CT2001A battery tester (Wuhan LANHE Inc.).

2.3. Microstructural observation

The anode products at a specified charge–discharge state were amassed after the battery cell was cooled to room temperature and sealed with epoxy. The samples were then characterized by SEM (Ultra Plus, ZEISS) and EDS (Shimadzu) for microstructural and elemental distribution analysis. XRD (MPDDY2094, PANalytical) was used to perform phase identification.

2.4. Elemental content analysis

After charging, the obtained anode products may contain several metallic elements such as Na, Ca, Zn, sodium oxides, calcium oxides, zinc oxides, $ZnCl_2$, NaCl, and $CaCl_2$ because of (1) oxidation of active metals when exposed to air; (2) the electrolyte adhesion on the surface.

According to the solubility differences of these substances in distinctive solvents, the contents of various substances in the anode products could be determined by a three-step dissolution method combined with elemental chemical analysis. The major experiment steps on elemental content analysis are described in Fig. 2. At last, the trace element contents (Na, Ca, Zn and Cl) in filtrates A, B, and C were analyzed using AAS (TAS-990). After discharging, the collected anode products were also tested by AAS.

2.5. Thermodynamic equilibrium calculations

FactSage software was used for thermodynamic calculations. The Na-Ca-Zn ternary phase diagram was derived from the calculation and binary phase diagrams of Na-Zn [38], Ca-Zn [39], and Na-Ca [40]. Furthermore, based on the Gibbs minimum free energy principle, the equilibrium cooling in the Equilib module was used to predict the phase transition for the cathode/anode products. In this study, the FactSage 7.2 version was used for the calculation, and the FTlite databases were used to calculate the phase equilibrium at 0.1 MPa. The temperature range is between 25 and 570 °C, with 10 °C intervals. The calculated results of FactSage were used as references for the experiment results.

3. Results and discussion

The voltage curves of the Na||Zn battery during charge–discharge are shown in Fig. 3(a). Only one discharge voltage plateau was observed at 40 and 100 mA cm^{-2}, while it exhibited four discharge potential plateaus at the current density of 10 mA cm^{-2}. At the beginning of discharge, the battery voltage dropped rapidly to 1.72 V due to ohmic resistance (IR), and then the voltage decreased slowly, showing the first discharge plateau. At point b in Fig. 3(a), the voltage suddenly dropped from 1.61 to 1.46 V, leading to the appearance of the second discharge plateau. Afterwards, the third (1.26 V) and fourth (0.91 V) discharge plateaus appeared, respectively. The cycling voltage of the battery at 10 mA cm^{-2} and the corresponding coulombic efficiency relationship are shown in Fig. 3(b). It depicts four discharge plateaus for each cycle, and the coulombic efficiency reached 80%.

To elaborate on the mechanisms, the electrode reactions at different charge–discharge states were considered by the thermodynamic analysis and phase diagram. Corresponding to the electrode reaction, the standard Gibbs free energy change at 560 °C was calculated by the thermodynamic software FactSage, and the standard cell voltage was obtained by Eq. (3).

$$\Delta G^{\theta}_{\text{cell}} = -zFE^{\theta}_{\text{cell}} \tag{3}$$

where G denotes the standard Gibbs free energy; z is the number of transferred electrons; F is the Faraday constant; E is the standard electromotive force.

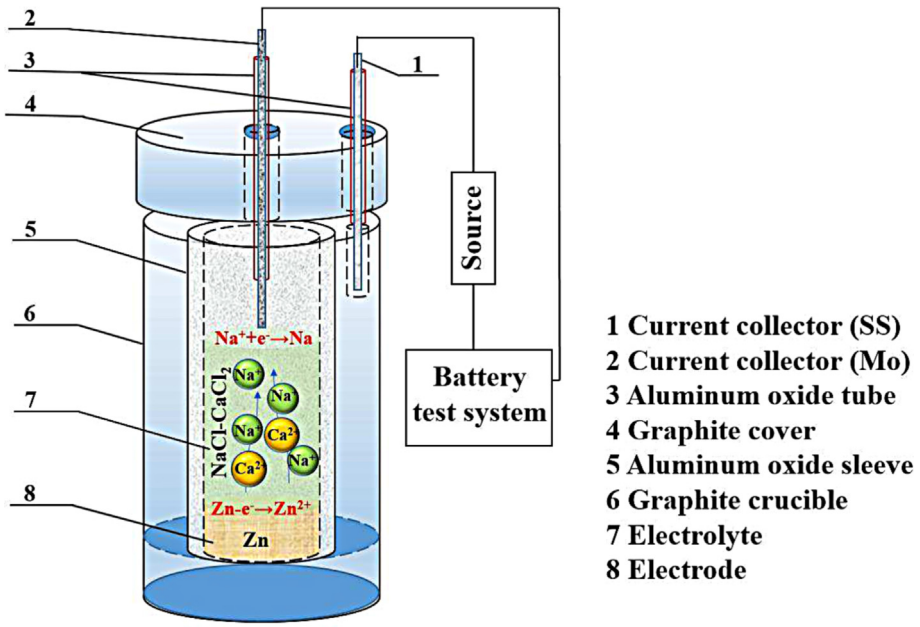

Fig. 1. Schematics of a Na||Zn LMB at a charging state.

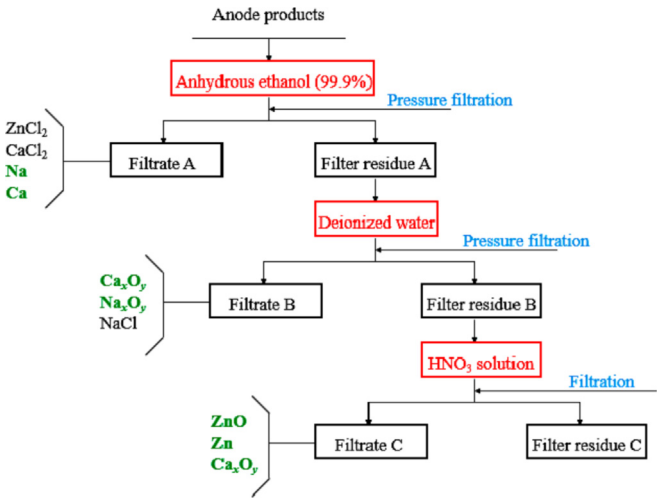

Fig. 2. Flow diagram of the anode products treatment process through three-step dissolution method.

At the beginning of the charging process, the possible electrode reactions are shown in the following Eqs. (4)–(6).

$$\text{Anode}: \mathrm{Zn} - 2e^- = \mathrm{Zn}^{2+} \tag{4}$$

$$\text{Cathode}: \mathrm{Na}^+ + e^- = \mathrm{Na} \tag{5}$$

$$\mathrm{Ca}^{2+} + 2e^- = \mathrm{Ca} \tag{6}$$

The cell reaction during the charging process is written as Eqs. (7) and/or (8), and the corresponding electromotive forces are written as Eqs. (9) and/or (10).

$$\mathrm{Zn(l)} + 2\mathrm{NaCl(l)} = \mathrm{ZnCl_2(l)} + 2\mathrm{Na(l)}, \qquad E_1^\theta = -1.871\ \mathrm{V} \tag{7}$$

$$\mathrm{Zn(l)} + \mathrm{CaCl_2(l)} = \mathrm{ZnCl_2(l)} + \mathrm{Ca(s)}, \qquad E_2^\theta = -1.897\ \mathrm{V} \tag{8}$$

$$E_1 = E_1^\theta - \frac{RT}{ZF}\ln K = E_1^\theta - \frac{RT}{ZF}\ln\frac{[\mathrm{ZnCl_2}][\mathrm{Na}]^2}{[\mathrm{NaCl}]^2[\mathrm{Zn}]} = E_1^\theta - \frac{RT}{2F}\ln[\mathrm{ZnCl_2}] + \frac{RT}{F}\ln[\mathrm{NaCl}] \tag{9}$$

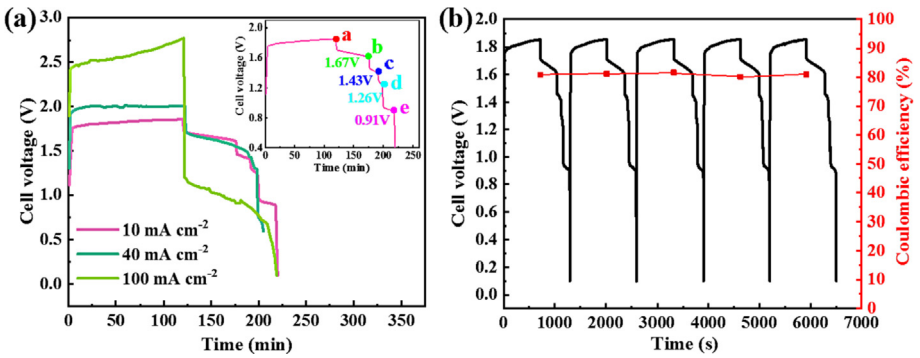

Fig. 3. Performance of a Na||Zn battery at 560 °C. (a) Voltage profiles during charge–discharge at different current densities (10–100 mA cm^{-2}) and (b) Coulombic efficiency and cell voltage as functions of cycle number at 10 mA cm^{-2}.

$$E_2 = E_2^{\theta} - \frac{RT}{ZF}\ln K = E_2^{\theta} - \frac{RT}{ZF}\ln\frac{[ZnCl_2][Ca]}{[CaCl_2][Zn]}$$
$$= E_2^{\theta} - \frac{RT}{2F}\ln[ZnCl_2] + \frac{RT}{2F}\ln[CaCl_2] \quad (10)$$

As the activity of NaCl and $CaCl_2$ are almost the same which is less than 1 in the equimolar NaCl-$CaCl_2$ molten salts, it can be deduced from Eqs. (9) and (10) that the reduction potential of Ca^{2+} is more negative than that of Na^+. Sodium is more easily electrodeposited in equal molar NaCl-$CaCl_2$ molten salts. However, as the reduction potential gap of Ca^{2+} and Na^+ is small, Ca is easily co-electrodeposited with Na metal during the charging process. This result is consistent with the fact that sodium with 4 wt% calcium metal is obtained in equal molar NaCl-$CaCl_2$ molten salts electrolyte for the sodium electrolysis industry [41].

With the progress of charging, Zn^{2+} which is produced on the cathode side diffuses into NaCl-$CaCl_2$ molten salts and simultaneously transfers to the anode side. Zn may be produced due to the chemical reaction and the electrochemical reduction reaction as shown in (11)–(13), which resulted in the decrease of capacity and coulombic efficiency. To enhance the capacity and coulombic efficiency, inhibiting the transfer or lowering the transfer rate of $ZnCl_2$ from the cathode side to the anode side is critical. The effect of cell structure, electrolyte composition, and even membrane need to be further done.

$$ZnCl_2(l) + 2Na(l) = Zn(l) + 2NaCl(l), \quad \Delta G^{\theta} = -361\ \text{KJ mol}^{-1} \quad (11)$$

$$ZnCl_2(l) + Ca(s) = Zn(l) + CaCl_2(l), \quad \Delta G^{\theta} = -366\ \text{KJ mol}^{-1} \quad (12)$$

$$Zn^{2+} + 2e^- = Zn \quad (13)$$

In pure sodium melt, the produced Zn will drop down to the cathode because of the highest density of Zn in the cell system and the de-alloy nature of Zn with Na metal at 560 °C. However, Ca-Zn alloy forms when Ca contacts with Zn.

During discharge, metallic Na and Ca on the anode side lost electrons and transformed into Na^+ and Ca^{2+}. The contents of Na and Ca gradually decreased as the discharge progressed, increasing the relative content of Zn in Ca-Zn alloy. When the relative content of Zn in Ca reaches 0.48 mol%, $CaZn_2$ solid phase will form and coat the surface of Mo wire. The direct contact of the remaining Ca with Mo wire was cut off when $CaZn_2$ alloy completely wrapped the Mo wire. The discharge process was turned to the extraction of Ca in $CaZn_2$ alloy, and $CaZn_3$, $CaZn_5$, and $CaZn_{13}$ were formed in succession according to the phase diagram [42–47]. The de-alloying process of Ca-Zn alloy is similar to the de-lithiation process in lithium-based LMBs [48–51].

The cell reactions are shown in reactions (14)–(17), respectively.

$$3CaZn_2(s) + ZnCl_2(l) = 2CaZn_3(s) + CaCl_2(l) + Zn(l), \quad E^{\theta} = 1.749\ \text{V} \quad (14)$$

$$5CaZn_3(s) + 2ZnCl_2(l) = 3CaZn_5(s) + 2CaCl_2(l) + Zn(l), \quad E^{\theta} = 1.740\ \text{V} \quad (15)$$

$$13CaZn_5(s) + 8ZnCl_2(l) = 5CaZn_{13}(s) + 8CaCl_2(l) + 8Zn(l), \quad E^{\theta} = 1.584\ \text{V} \quad (16)$$

$$CaZn_{13}(s) + ZnCl_2(l) = 14Zn(l) + CaCl_2(l), \quad E^{\theta} = 1.246\ \text{V} \quad (17)$$

It can be seen from the above equations that the electromotive force of the reaction (14) was almost equal to the reaction (15). Therefore, the battery voltage did not change obviously with the electrode reaction. Both of them occurred in the second discharge plateau, and reactions (16) and (17) were responsible for the third and fourth discharge plateau, respectively.

To verify the above deduction, the cathode/anode products at different charge–discharge states (marked as a, b, c, d, and e in Fig. 3a) were collected when the battery cell was cooled down to room temperature, and characterized by SEM and XRD. As phase transformation may occur during the cooling process, the detected substance after cooling was different from that at the battery cell temperature (560 °C). The phase transitions of the products at different charge–discharge states in the cooling process were also analyzed by the Na-Ca-Zn ternary phase diagram.

Fig. 4(a) is the photograph of the Mo wire, and the battery cell, which is cooled when the cell is fully charged (point a state in Fig. 3a). There was no adherent on the Mo wire surface. Moreover, there was a piece of white matter on the electrolyte's surface and a metallic luster substance in the upper layer. Fig. 4(b–d) is the SEM image of the metallic luster substance. It can be seen from Fig. 4(c) that it was divided into bright gray and dark gray regions. The element distribution map showed (Fig. 4d) that there are Na, Zn, Ca, and O elements in the bright gray region and Ca and O elements in the dark gray region. The existence of the O element was caused by the oxidation of metal exposed to the air during the SEM sample preparation [15]. The distribution of major element Ca dendritic, which illustrates the Ca's segregation of metallic Ca during the cooling process. Moreover, as shown in Fig. S1, the metallic luster substance was mainly composed of Ca elements. Compared to the product which was produced at 200 mA cm^{-2} after the battery has run for 20 days in ref. [34], there is less Zn content in the anode product in this study, suggesting Zn cumulative aggregated in the anode side during cycling since some Zn element cannot be all converted to Zn^{2+} in the discharge process. Moreover, no aluminum element was detected here since the product is collected in the first cycle, and the corrosion of the Al_2O_3 tube can be ignored.

Figs. S2–S9 show the photograph of the Mo wire and the cross-section SEM images as well as EDS results of the anodic product, which were taken at the point of b, c, d, and e states in Fig. 3(a), respectively. As shown in Fig. S2, some adhesive materials on the Mo wire were taken out at the end of the first discharge plateau (point b in Fig. 3a). The dendritic metallic Ca disappeared, and the bright gray region in Fig. 4(c) broke into small pieces, as shown in Fig. S2. Moreover, the dark gray region area decreased with further discharge, as shown in Figs. S2–S9.

Fig. 5 shows the XRD patterns of the collected metallic luster substance (point a state) and the adherence on Mo wire at points b, c, d, and e states, respectively. Metallic Zn, metallic Ca, hydroxide (NaOH and $Ca(OH)_2$), Ca_2CO_3, Ca_3Zn, and Ca_5Zn_3 phases were observed in the collected metallic luster substance. The appearance of hydroxides and carbonates is attributed to the moisture absorption of the sample exposed to air during testing. The cooled anode product at point b state was composed of Ca_5Zn_3, Ca_3Zn, and $CaZn_2$, while $CaZn_3$, $CaZn_5$, and $CaZn_2$ were detected at point c state. $NaZn_{13}$, $CaZn_{13}$, $CaZn_3$, $CaZn_5$ and Zn, $NaZn_{13}$, $CaZn_{13}$, $CaZn_5$, $CaZn_2$ were observed for the anode product at points d and e, respectively.

Table S1 shows the relative elemental content of the detected substance analyzed by the AAS method. The phase of anode products at points a, b, c, d, and e states are shown in Fig. 6. For Fig. 6, the Na-Ca-Zn ternary phase diagram and the phase in each region are obtained using the figure module of FactSage 7.2 software. Here, L is a homogeneous liquid phase, L_1, as well as L_2, are immiscible liquid phases, and all of them are composed of different relative contents of Na, Ca, and Zn metal. BCC is Ca solid solution with dissolved Na. The position of a-e points in the ternary phase diagram is plotted based on the data in Table S1.

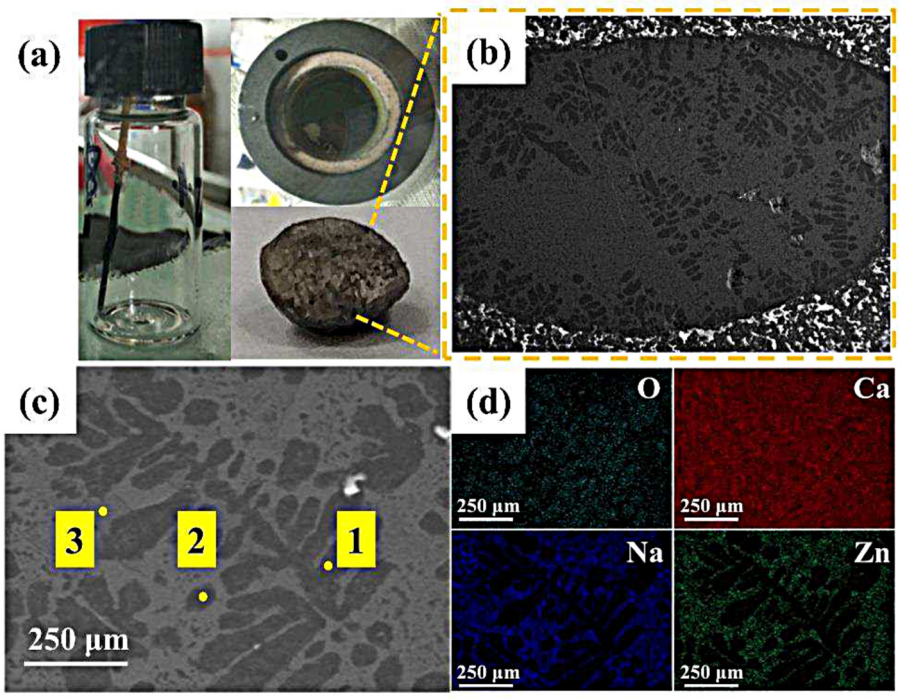

Fig. 4. (a) Photograph of anode products after fully charged; (b–d) the microstructure and elemental distribution in the cross-section of anode products.

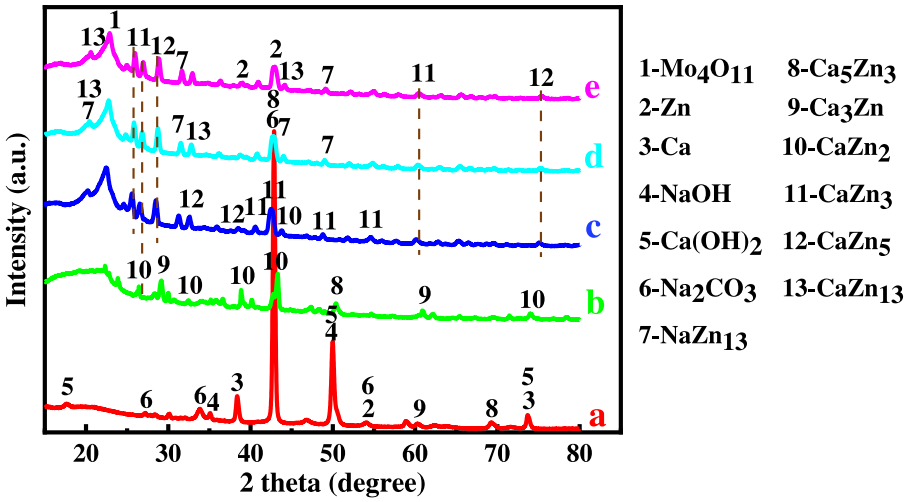

Fig. 5. XRD patterns of anode products in Na||Zn battery at room temperature (The letters a, b, c, d, and e correspond to the voltage curves in Fig. 3 for different states).

As shown in Fig. 6, point a was composed of L_1 + L_2 + BCC at 560 °C, while it consisted of L_1 + L_2 + $CaZn_2$, L_1 + $CaZn_3$ + $CaZn_5$, L_1- + $NaZn_{13}$ + $CaZn_{13}$, and L_1 + $NaZn_{13}$ + $CaZn_{13}$ in b, c, d, e point states, respectively. Specific phase components of the anode products at different charge–discharge states at 560 °C are shown in Table S2. In point a state, L_1 was composed of Na-Ca-Zn (0.0216–0.1639–0.0301 mol%), which was consistent with point 3 (Fig. S1). Interestingly, BCC was made up of Na-Ca-Zn (0.0281–0.6724–0.0009 mol%), which was coincident with points 1 and 2 (Fig. S1). It can be deduced that L_1 and BCC represent the metallic luster substance (Fig. 4a). L_2 was formed with Na-Ca-Zn (0.0820–0.0009–0.00001 mol%); it may be the white matter on the surface of the electrolyte (Fig. 4a). In a word, the anode products after charging were consistent with phase composition in Na-Ca-Zn ternary phase diagram.

Fig. 7 presents the phase transformation of anode products in cooling process using FactSage thermodynamics software. The specific composition of the phase in different charge–discharge state at 25 °C is shown in Table S3. The phase transformation equations were described as follows:

a: L_1 + L_2 + BCC → FCC + BCC + Ca_3Zn

b: L_1 + L_2 + $CaZn_2$ → CaZn + BCC + $CaZn_2$

c: L_1 + $CaZn_3$ + $CaZn_5$ → Na (l) + $CaZn_3$ + $CaZn_5$ → BCC + $CaZn_3$ + $CaZn_5$

d: L_1 + $CaZn_{13}$ + $NaZn_{13}$ → $NaZn_{13}$ + $CaZn_{11}$ + $CaZn_{13}$

e: L_1 + $CaZn_{13}$ → HCP + $CaZn_{13}$ + $NaZn_{13}$

Here, HCP is zinc solid solution.

By the consideration of electrode reaction and phase transformation, the possible phase of the cooled product at different charge–discharge states are listed in Table 1. As a comparison,

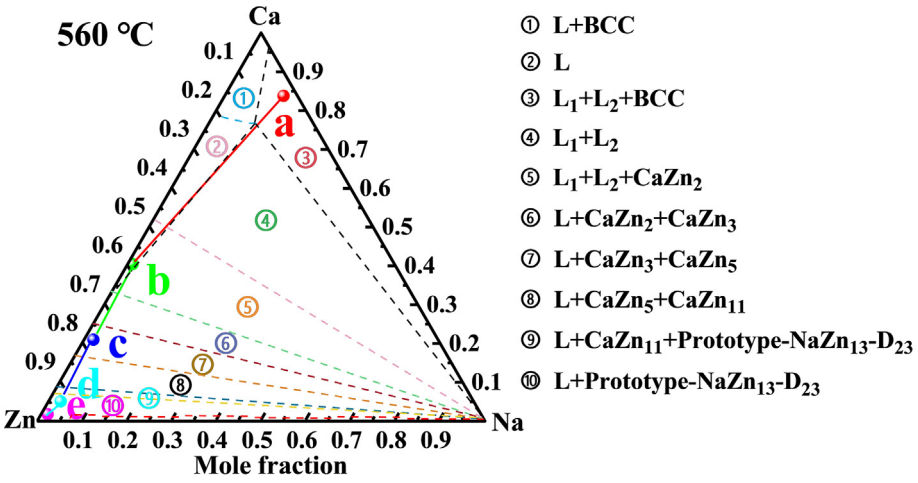

Fig. 6. Phase evolution in the discharge process of the Na|NaCl-$CaCl_2$|Zn liquid metal battery at 560 °C.

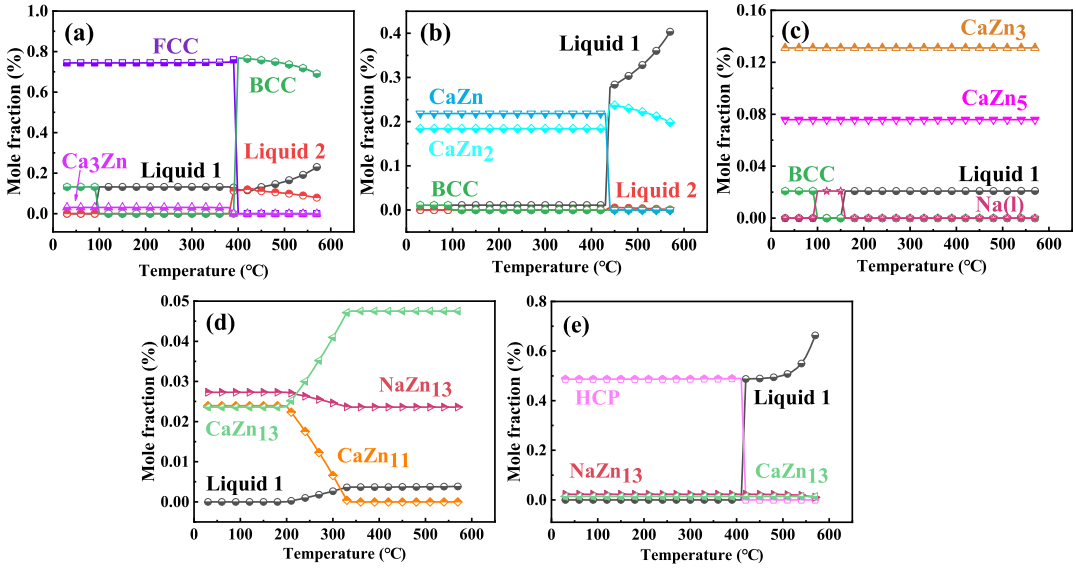

Fig. 7. FactSage calculates the change of solid phase precipitation during equilibrium cooling of the anode products at different states (as shown in Fig. 3).

the detected phases by XRD were also listed. However, CaZn and $CaZn_{11}$ phases were not observed in the XRD pattern because some Ca-Zn alloys have low formation rates [52]. It can be seen that the detected phases mainly are consistent with the substances by equilibrium analysis, indicating the theoretical deduction for the electrode reaction is reasonable.

Fig. 8 presents a schematic diagram for the phase evolution of anode products during charge–discharge processes. During the charging process, unmixable liquid Na and Ca metal layers with dissolved liquid Zn were produced at the anode half-cell. During discharge, Na and Ca metals lost electrons, and the contents of Na and Ca in the liquid metal layers gradually decreased with the increase of discharge deep, resulting in the enhancement of the relative content of dissolved Zn in the liquid Na and Ca layers. When the relative content of Zn in Ca reached 0.48 mol%, solid intermetallic $CaZn_2$ was obtained.

The direct contact between the liquid metal Ca and Mo wire was cut off when the generated $CaZn_2$ alloy entirely wrapped around the Mo wire, and this situation engendered a discharge of $CaZn_2$ by forming $CaZn_3$ and Ca^{2+}, which previously was responsible for the second discharge voltage plateau. Similarly, $CaZn_3$, $CaZn_5$, and $CaZn_{13}$ alloys were precipitated in succession because of the further discharge of Ca in Ca-Zn alloy. Finally, Ca in Ca-Zn alloy was consumed, and the battery cell voltage dropped to zero when the remaining Zn started to discharge, arriving at the end of discharge.

Table 1
The possible phases of the cooling products at different charge–discharge states.

State	A substance obtained by the analysis of the phase diagram	Detected substance by XRD
Point a	FCC, BCC, Ca_3Zn	Na, Ca, Zn, Na_2CO_3, NaOH, $Ca(OH)_2$, Ca_5Zn_3, Ca_3Zn
Point b	BCC, CaZn, $CaZn_2$	Ca_5Zn_3, Ca_3Zn, $CaZn_2$
Point c	BCC, $CaZn_3$, $CaZn_5$,	$CaZn_3$, $CaZn_5$, $CaZn_2$
Point d	$NaZn_{13}$, $CaZn_{11}$, $CaZn_{13}$,	$CaZn_{13}$, $CaZn_3$, $CaZn_5$, $NaZn_{13}$
Point e	HCP, $NaZn_{13}$, $CaZn_{13}$	Zn, $CaZn_{13}$, $CaZn_5$, $CaZn_2$, $NaZn_{13}$

It is worth noting that only one discharge voltage plateau appeared in the discharge process, as shown in Fig. 3(a) when

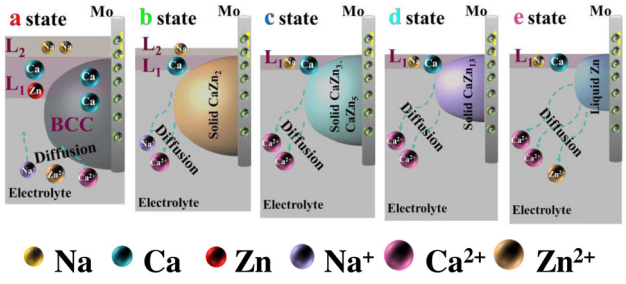

Fig. 8. Schematic diagram of the discharge process in Na||Zn battery.

the current density was greater than 10 mA cm^{-2}, indicating there is less Zn produced on the anode side at a higher charge current density. As we know, compare to Na^+ or Ca^{2+}, Zn^{2+} is more likely reduced to Zn since the reduction potential of Zn^{2+}/Zn is more positive than that of Na^+ /Na and Ca^{2+}/Ca. However, in Na|$CaCl_2$-NaCl|Zn battery, $ZnCl_2$ is produced on the cathode side at the bottom of the cell during the charging process, and it is unfavorable to transfer to the upper anode side since the $ZnCl_2$-NaCl-$CaCl_2$ mixture has a higher density than NaCl-$CaCl_2$ mixture. Higher ratio of $ZnCl_2$ in $ZnCl_2$-NaCl-$CaCl_2$ results in a higher density of melt and a slower transfer rate of $ZnCl_2$. More Na^+ or Ca^{2+} ions take part in the electro-reduction process to support the supplied high current density when the electro-reduction of Zn^{2+} in the anode side is limited by the transfer rate of Zn^{2+}. No Na or Ca is produced if the electron transfer induced by the electro-reduction of Zn^{2+} can support the supplied current density. In our previous reports, it also has been proved that higher coulombic efficiency can be gotten at higher current density [34], suggesting less content of Zn is reduced at higher charge current density.

4. Conclusions

In this study, a treatment process of anode product through atomic absorption spectrometry analysis was proposed and has shown for the first time that the anode in Na|NaCl-$CaCl_2$|Zn LMB after charging is composed of unmixable liquid metallic Na (upper layer) and metallic Ca layer (lower layer) with a certain content of dissolved Zn. The discharge of Na/Ca is responsible for the first discharge plateau, while the extraction of Ca in $CaZn_2$, $CaZn_3$, $CaZn_5$, and $CaZn_{13}$ alloys corresponds to the successive discharge voltage plateaus, respectively. Higher current density results in the lower content of Zn in the anode, which shortens the discharge time of the extraction of Ca in Ca-Zn alloys.

Declaration of competing interest

The authors declare that they have no known competing financial interests or personal relationships that could have appeared to influence the work reported in this paper.

Acknowledgments

The authors are grateful for the financial support from the National Natural Science Foundation of China (52074084) and the Guangxi Innovation-driven Development Program, China (GUIKE AA18118030).

Appendix A. Supplementary data

Supplementary data to this article can be found online at https://doi.org/10.1016/j.jechem.2022.04.035.

References

[1] K.Z. Rinaldi, J.A. Dowling, T.H. Ruggles, K. Caldeira, N.S. Lewis, Environ. Sci. Technol. 55 (2021) 6214–6226.
[2] W. Weng, B.M. Jiang, Z. Wang, W. Xiao, Sci. Adv. 6 (2020) 1–7.
[3] S.X. Jing, M.Y. Wang, W. Xiao, Energy Chem. 64 (2022) 404–405.
[4] W. Zhang, D. Wang, W.T. Zheng, J. Energy Chem. 41 (2020) 100–106.
[5] L.Y. Kong, L.Y. Liao, H.W. Zhang, J.W. Zhao, Electrical Switches 46 (2008) 61–62.
[6] X.Y. Shen, Z.Q. Huang, J.X. Zhou, L. Zhou, Power Technology 35 (2011) 602–604.
[7] S.L. Zhang, Y. Zheng, X.J. Huang, J. Hong, B. Cao, J.N. Hao, Q.N. Fan, T.F. Zhou, Z.P. Guo, Adv. Energy Mater. 9 (2019) 1900081.
[8] Y.Y. Liu, Y.Y. Zhu, Y. Cui, Nat. Energy 4 (2019) 540–550.
[9] W. Weng, J.X. Xiao, Y.J. Shen, X.X. Liang, T. Lv, W. Xiao, Angew. Chem. Int. Ed. 60 (2021) 24905–24909.
[10] T. Lv, J.X. Xiao, W. Weng, W. Xiao, Adv. Energy Mater. 10 (2020) 2002241.
[11] H. Kim, D.A. Boysen, J.M. Newhouse, B.L. Spatocco, B. Chung, P.J. Burke, D.J. Bradwell, K. Jiang, A.A. Tomaszowska, K.L. Wang, W.F. Wei, L.A. Ortiz, S.A. Barriga, S.M. Poizeau, D.R. Sadoway, Chem. Rev. 113 (2013) 2075–2099.
[12] D.J. Bradwell, H. Kim, A.H. Sirk, D.R. Sadoway, J. Am. Chem. Soc. 134 (2012) 1895–1897.
[13] H.M. Li, H.Y. Yin, K.L. Wang, S.J. Cheng, K. Jiang, D.R. Sadoway, Adv. Energy Mater. 6 (2016) 1600483.
[14] E.J. Cairns, C.E. Crouthamel, A.K. Fischer, M.S. Foster, J.C. Hesson, C.E. Johnson, H. Shimotake, A.D. Tevebaugh, ANL-7316, Argonne National Lab, Chicago, 1967, pp. 27–37.
[15] J.L. Sudworth, J. Power Sources 100 (2001) 149–163.
[16] R.D. Weaver, S.W. Smith, N.L. Willmann, J. Electrochem. Soc. 109 (1962) 653–657.
[17] B. Agruss, H.R. Karas, In Regenerative EMF Cells 64 (1967) 62–81.
[18] L.A. HerÉDy, M.L. Iverson, G.D. Ulrich, H.L. Recht, In Regenerative EMF Cells 64 (1967) 30–42.
[19] I.J. Groce, R.D. Oldenkamp, In Regenarative EMF Cells 64 (1967) 43–52.
[20] R.D. Oldenkamp, H.L. Recht, In Regenerative EMF Cells 64 (1967) 53–61.
[21] J. McDowall, J. Power Sources 162 (2006) 959–964.
[22] K.L. Wang, K. Jiang, B. Chung, T. Ouchi, P.J. Burke, D.A. Boysen, D.J. Bradwell, H. Kim, U. Muecke, D.R. Sadoway, Nature 514 (2014) 348–350.
[23] H.M. Li, K.L. Wang, S.J. Cheng, K. Jiang, ACS Appl. Mater. Interfaces 8 (2016) 12830–12835.
[24] H.Y. Yin, B. Chung, F. Chen, T. Ouchi, J. Zhao, N. Tanaka, D.R. Sadoway, Nat. Energy 3 (2018) 127–131.
[25] K. Mushtaq, J. Zhao, N. Weber, A. Mendes, D.R. Sadoway, J. Energy Chem. 66 (2022) 390–396.
[26] T. Ouchi, H. Kim, B.L. Spatocco, D.R. Sadoway, Nat. Commun. 7 (2016) 10999.
[27] N.E. Holubowitch, S.E. Manek, J. Landon, C.A. Lippert, S.A. Odom, K.L. Liu, Adv. Mater. Technol. 1 (2016) 1600035.
[28] T. Dai, Y. Zhao, X.H. Ning, R. Lakshmi Narayan, J. Li, Z.W. Shan, J. Power Sources 381 (2018) 38–45.
[29] J. Kim, D. Shin, Y. Jung, S.M. Hwang, T. Song, Y. Kim, U. Paik, J. Power Sources 377 (2018) 87–92.
[30] W. Zhao, P. Li, K. Han, K.X. Cui, C.R. Liu, Q.W. Tan, X.H. Qu, J. Power Sources 463 (2020) 228233.
[31] H.M. Li, K.L. Wang, H. Zhou, X.L. Guo, S.J. Cheng, K. Jiang, Energy Stor. Mater. 14 (2018) 267–271.
[32] E.J. Cairns, H. Shimotake, Science 164 (1969) 1347–1355.
[33] T. Weier, A. Bund, W. El-Mofid, G.M. Horstmann, C.C. Lalau, S. Landgraf, M. Nimtz, M. Starace, F. Stefani, N. Weber, IOP Conf. Ser, Mater. Sci. Eng. 228 (2017) 012013.
[34] J.L. Xu, O.S. Kjos, K.S. Osen, A.M. Martinez, O.E. Kongstein, G.M. Haarberg, J. Power Sources 332 (2016) 274–280.
[35] J.L. Xu, A.M. Martinez, K.S. Osen, O.S. Kjos, O.E. Kongstein, G.M. Haarberg, J. Electrochem. Soc. 164 (2017) A2335–A2340.
[36] Y.S. Li, M. Spiegel, S. Shimada, Mater. Chem. Phys. 93 (2005) 217–223.
[37] W.J. Ding, H. Shi, A. Jianu, Y.L. Liu, A. Bonk, A. Weisenburger, T. Bauer, Sol. Energ. Mat. Sol. C. 193 (2019) 298–313.
[38] Y.J. Liu, Y. Ge, D. Yu, J. Alloys Compd. 476 (2009) 79–83.
[39] S. Wasiur-Rahman, M. Medraj, Intermetallics 17 (2009) 847–864.
[40] A.D. Pelton, Bull. Alloy Phase Diagrams 6 (1985) 35.
[41] D. Aurbach, Nonaqueous Electrochemistry, Marcel Dekker, New York, 1999.
[42] A.F. Messing, M.D. Adams, R.K. Steunenberg, Trans. ASM 56 (1963) 345–350.
[43] V.P. Itkin, C.B. Alcock, J. Phase Equilib. 11 (1990) 328–333.
[44] M.L. Fornasini, F. Merlo, Acta Crystallogr, Sect. B: Struct. Crystallogr. Cryst. Chem. 36 (1980) 1739–1744.
[45] Z.W. Yang, D.M. Shi, B. Wen, R. Melnik, J. Alloys Compd. 524 (2012) 53–58.
[46] C.O. Brubaker, Z.K. Liu, Calphad 25 (2001) 381–390.
[47] J. Delcet, J.J. Egan, Metall. Trans. B 9 (1978) 728–729.
[48] W. Zhao, P. Li, Z.W. Liu, D.L. He, K. Han, H.L. Zhao, X.H. Qu, Chem. Mater. 30 (2018) 8739–8746.
[49] H.L. Xie, H.L. Zhao, J. Wang, P. Chu, Z. Yang, C.Q. Han, Y.C. Zhang, J. Power Sources 472 (2020) 228634.
[50] W.M. Li, H. Shi, K.F. Du, W. Liu, H.Y. Yin, K. Jiang, D. Wang, J. Electroanal. Chem. 901 (2021) 115719.
[51] S. Yan, X.B. Zhou, H.M. Li, Y. Shen, Y.L. He, H. Zhou, K.L. Wang, K. Jiang, J. Power Sources 514 (2021) 230578.
[52] T. Nohira, H. Kambara, K. Amezawa, Y. Ito, J. Electrochem. Soc. 152 (2005) C183–C189.